Earth and Planetary Science Letters 456 (2016) 168–181

Contents lists available at ScienceDirect

Earth and Planetary Science Letters

www.elsevier.com/locate/epsl

River network evolution as a major control for orogenic exhumation: Case study from the western Tibetan plateau

Loraine Gourbet [a,e,*], Gweltaz Mahéo [a], David L. Shuster [b,c], Alka Tripathy-Lang [b,c], Philippe Hervé Leloup [a], Jean-Louis Paquette [d]

[a] Univ Lyon, Ens de Lyon, Univ Lyon 1, CNRS, UMR 5276 LGL-TPE, F-69342, Lyon, France
[b] Department of Earth and Planetary Science, University of California, Berkeley, 479 McCone Hall, Berkeley, CA 94720-4767, USA
[c] Berkeley Geochronology Center, 2455 Ridge Road, Berkeley, CA 94709, USA
[d] Laboratoire Magmas et Volcans, 5 rue Kessler, 63038 Clermont-Ferrand, France
[e] Geologisches Institut, ETH, Zürich, Switzerland

ARTICLE INFO

Article history:
Received 2 May 2016
Received in revised form 19 September 2016
Accepted 21 September 2016
Available online 20 October 2016
Editor: A. Yin

Keywords:
western Tibetan plateau
geomorphology
(U–Th–Sm)/He and ^{4}He/^{3}He thermochronometry
internal drainage

ABSTRACT

The westernmost Tibetan plateau, despite being internally drained, has a high topographic relief. Here, using apatite (U–Th–Sm)/He and ^{4}He/^{3}He thermochronometry, we reconstruct the exhumation history of the Rutog batholith during the Neogene. Thermal modeling in 1D using the QTQt program indicates that relatively slow cooling occurred from 30 Ma to 19 Ma, which we interpret as an exhumation rate of ~10 m/Ma. This was followed by two pulses of moderate cooling from 19 to 17 Ma and ~11 to 9 Ma that correspond to a total exhumation of about 1500 m. Cooling since 9 Ma has been negligible. This differs from exhumation patterns in central Tibet but reveals timing similarities with externally drained portions of southern Tibet. We interpret our cooling constraints as recording two different transitions in western Tibet from an externally to an internally drained system since the Oligocene. External drainage allowed this part of the Tibetan plateau, unlike internally drained portions of central Tibet, to record regional-scale processes. The first cooling event, at about 20 Ma, was likely related to a major geodynamic event such as slab breakoff that induced contemporaneous potassic and ultrapotassic magmatism. The second rapid cooling pulse from ~11 Ma to 9 Ma and subsequent negligible cooling was most likely controlled by a local factor such as Indus and Shyok river network reorganization caused by dextral motion of the Karakorum fault. We discuss these interpretations and their limitations in this contribution.

1. Introduction

Tibet, the highest and widest plateau on Earth, is usually described as a high elevation, low relief geomorphic feature. However, relief (i.e. elevation difference between the highest and lowest points in a given area) is not uniform across the plateau, with distinct morphological contrast between different parts of Tibet (Fielding et al., 1994; Liu-Zeng et al., 2008).

Central Tibet has the lowest relief compared to the rest of the plateau, likely because it is internally drained (Fig. 1a) and has low precipitation rates (Liu-Zeng et al., 2008). The internal drainage favors low relief because of internal deposition, which tends to smooth topography. Areas with significant relief (>2 km) are limited to active rifts, such as the Nyainqentanglha range (Armijo et al., 1989). Early studies (Shackleton and Chang, 1988) suggest that low relief formed in central Tibet from middle to late Miocene and corresponds to an erosion surface. However, for northern central Tibet (Qiangtang block) Rohrmann et al. (2012) suggest that a transition from a fast to slow exhumation regime, similar to the modern one, occurred during Late Cretaceous–early Cenozoic times. Haider et al. (2013) reconstruct a similar exhumation history for the southern part of central Tibet (Lhasa block), and using thermochronology, Hetzel et al. (2011) suggest that the low-relief surface on the northern Lhasa block formed before 50 Ma. In addition, paleoelevation studies imply that central Tibet was already near its present elevation by late Eocene (for a review, see Quade et al., 2011). Thus, modern elevation and relief in central Tibet might have been reached by 45 Ma.

In the southern, externally drained plateau margin, Tremblay et al. (2015) use thermochronometry data from the eastern Lhasa terranes to propose that the landscapes are the result of a major reorganization of the river network between 10 and 15 Ma. This modification consisted of a transition from N–S transverse rivers flowing from the plateau margin across the Himalaya, to longitudi-

* Corresponding author at: Geologisches Institut, ETH, Zürich, Switzerland.
E-mail address: loraine.gourbet@ens-lyon.fr (L. Gourbet).

http://dx.doi.org/10.1016/j.epsl.2016.09.037
0012-821X/

nal E–W rivers with lower channel slope and stream power flowing parallel to the Yarlong Suture zone (Tremblay et al., 2015). This river diversion allowed the sustainability of low-erosion conditions that are characteristic of the plateau.

In this work, we focus on western Tibet, which has thus far not been studied in detail. Unlike central Tibet, western Tibet has high relief of approximately 1.8 km, with mean and peak elevations of ~5100 and 6400 m, respectively. The main geomorphic features are E–W trending flat-floored valleys that are up to 120 km long. Like central Tibet, it is mostly internally drained. It is also the driest part of the plateau. Precipitation is less than 100–200 mm/yr (Domroes and Peng, 1988; Maussion et al., 2014).

There are a few active N–S rifts in this region, like in the rest of the Tibetan plateau (Fig. 1b). They affect relief at a local scale only and they are not the origin of the regional high relief (Gourbet et al., 2015). The only major tectonic feature that strongly influences topography is the Karakorum fault, which does not belong to the plateau *sensu stricto* because it forms the boundary between the western plateau and the Ladakh and Karakorum ranges. Local active strike-slip faults do not affect landscape, except for the dextral Bangong Co fault (BCF) that is responsible for the shape of the 40-km-long southeastern portion of the Bangong Lake (Fig. 1b). In other words, minor tectonic activity and modern precipitation cannot explain such high relief. The presence of high relief in western Tibet raises the question of the possible influence of an older, inherited relief on the present topography. Gourbet et al. (2015) suggest that the deep E–W trending valleys belong to an inherited paleotopography that formed prior to Oligocene time, when the western Tibetan plateau was externally drained. By late Oligocene time, these valleys were filled, at least partially, with red continental alluvial fan sediments that today are exposed along their flanks. Because these fans have been partially eroded away and this missing detritus is not present on the plateau, it suggests a second episode of external drainage since the Oligocene (Gourbet et al., 2015). These authors further hypothesize that a drainage reorganization occurred when the externally drained western Tibetan plateau transitioned at ca. 4 Ma to the internally drained regime that exists today. An externally drained area is sensitive to geodynamic processes; for example, river incision can respond to uplift variations. If the hypothesis that western Tibet was externally drained at times in the past is correct, then western Tibet was sensitive to the geodynamic evolution of the plateau and can provide useful information not only regarding its local history, but also the general history of the whole plateau. Here, we focus on examining the relief evolution of the westernmost Tibetan plateau by quantifying the exhumation history of this region in the Rutog and Shiquanhe area. We use apatite (U–Th–Sm)/He and $^{4}He/^{3}He$ thermochronometry, and infer exhumation rates that are converted into erosion rates.

2. Geologic setting of western Tibet

Western Tibet is bounded by the Tarim basin to the north, by the Karakorum range to the west and the Gangdese arc to the south (Fig. 1a). This study focuses on the area encompassing the Lhasa and Qiangtang blocks, between the Longmu–Gozha Co left-lateral strike-slip fault system (LGCF) and the active dextral strike-slip Karakorum Fault Zone (KFZ) that bounds the Karakorum, Bangong, Ladakh and Ayilari ranges (Fig. 1b). The LGCF separates the Qiangtang bock to the south from the Tianshuihai block to the North (Tapponnier and Molnar, 1977; Matte et al., 1996; Leloup et al., 2012). It is the westernmost (Liu, 1993) and youngest (Chevalier et al., 2015) segment of the active Altyn Tagh strike-slip fault system. According to Raterman et al. (2007), the LGCF was activated at *ca* 9 Ma and interacts not only with the Altyn Tagh fault, but also with the KFZ, the LGCF intersecting the KFZ and thus forming a triple junction separating the NW Himalaya, the Tianshuihaï block, and the western Tibetan plateau. The KFZ extends for 1000 km and is related to the eastward extrusion of the plateau (Tapponnier and Molnar, 1977; Tapponnier et al., 1982). Recent estimates of the total offset range from ~50 km (Murphy et al., 2000) to ~250 km (Leloup et al., 2013; Gourbet et al., 2015) and its initiation in the Shiquanhe area ranges from before 23 Ma (Lacassin et al., 2004; Valli et al., 2007, 2008) to 17–14 Ma (Phillips et al., 2004; Murphy et al., 2009). Locally the KFZ also has a component of normal motion, as evidenced by >300 m-high facets facing the Tibetan plateau in the Ladakh and Ayilari ranges. In the Ayilari range, the normal motion has been dated to 14 Ma using feldspar, muscovite and biotite $^{40}Ar/^{39}Ar$ and apatite (U–Th–Sm)/He thermochronology (Valli et al., 2007). Van Buer et al. (2015) propose that the N-S normal Angmong fault connects to KFZ and the LGCF (Fig. 1b) and would be the surface expression of ~E–W Miocene ductile flow in the lower crust.

Western Tibet terranes are dominated by Paleo-Mesozoic sediments (Fig. 1b), e.g. limestones (Carboniferous to Triassic), flyschoid shales (Jurassic) and conglomerates (Triassic) (Matte et al., 1996; Pan et al., 2004). These terranes are overlayed by rare continental red sandstones and conglomerates (red beds). Absolute dating of interbedded and underlying ultrapotassic lava flows indicate a late Oligocene-early Miocene age for the red beds deposition near Shiquanhe (Arnaud, 1992; Kapp et al., 2003; Williams et al., 2004; Gourbet et al., 2015) and a pre-35 Ma deposition age near Rutog (Cheng and Xu, 1987). However, analysis of detrital zircons contained in the red beds performed by Raterman et al. (2007) further north in the Domar area indirectly suggests a Jurassic deposition age. Magmatic rocks in western Tibet are dominated by granitoid plutons of Jurassic (Pan et al., 2004) and Cretaceous (Matte et al., 1996; Pan et al., 2004) ages. Volcanic rocks consist of ultrapotassic lavas mentioned above, and Jurassic basalts (Qiangtang block, Arnaud and Vidal, 1990).

The study area experienced a multi-stage deformation history. An early Paleozoic stage is recorded in the Qiangtang block and is interpreted to be related to the northern Gondwana-Asia convergence (Raterman et al., 2007). It was followed by a poorly understood late Paleozoic deformation phase (Matte et al., 1996; Kapp et al., 2003; Raterman et al., 2007). The main Mesozoic shortening event corresponds to the Lhasa-Qiangtang collision; it occurred during the Late Jurassic-Late Cretaceous and is responsible for significant N–S shortening in the Domar fold-and-thrust belt (Raterman et al., 2007). Emplacement of the Rutog batholith occurred at ~80 Ma (Zhao et al., 2008). Afterwards, the India–Asia collision led to Cenozoic ~NS shortening that induced ~EW trending structures, including the Jaggang and Shiquanhe thrusts and the Risum anticlinorium (Fig. 1b). The Jaggang thrust, which bounds the Risum anticlinorium to the south, is believed to have absorbed >40 km of shortening in the late Cretaceous–early Mesozoic times (Kapp et al., 2003). Because ophiolites are found north and south of the Risum anticlinorium (Fig. 1b), Matte et al. (1996) interpreted it as a microcontinental block sandwiched between two north-dipping subductions: the Bangong one to the north (Early Cretaceous) and the Shiquanhe one to the south (Late Cretaceous). After that interpretation, the Shiquanhe suture would be the equivalent of the Shyok suture (Late Cretaceous), located west of the KFZ. This implies a ≥200 to 240 km offset due to the KFZ (Valli et al., 2008). Alternatively, Kapp et al. (2003) suggest that the Risum anticlinorium belongs to the basement of the Lhasa block and that the two ophiolitic belts correspond to a single suture zone, i.e. the Bangong suture zone. This interpretation would imply that the Shyok suture would have no counterpart on the other side of the KFZ. The Shiquanhe thrust is ~E–W trending, dips 20°N and truncates Cenozoic conglomerates (Fig. 1b). These conglomerates are interbedded with previously mentioned lava flows that

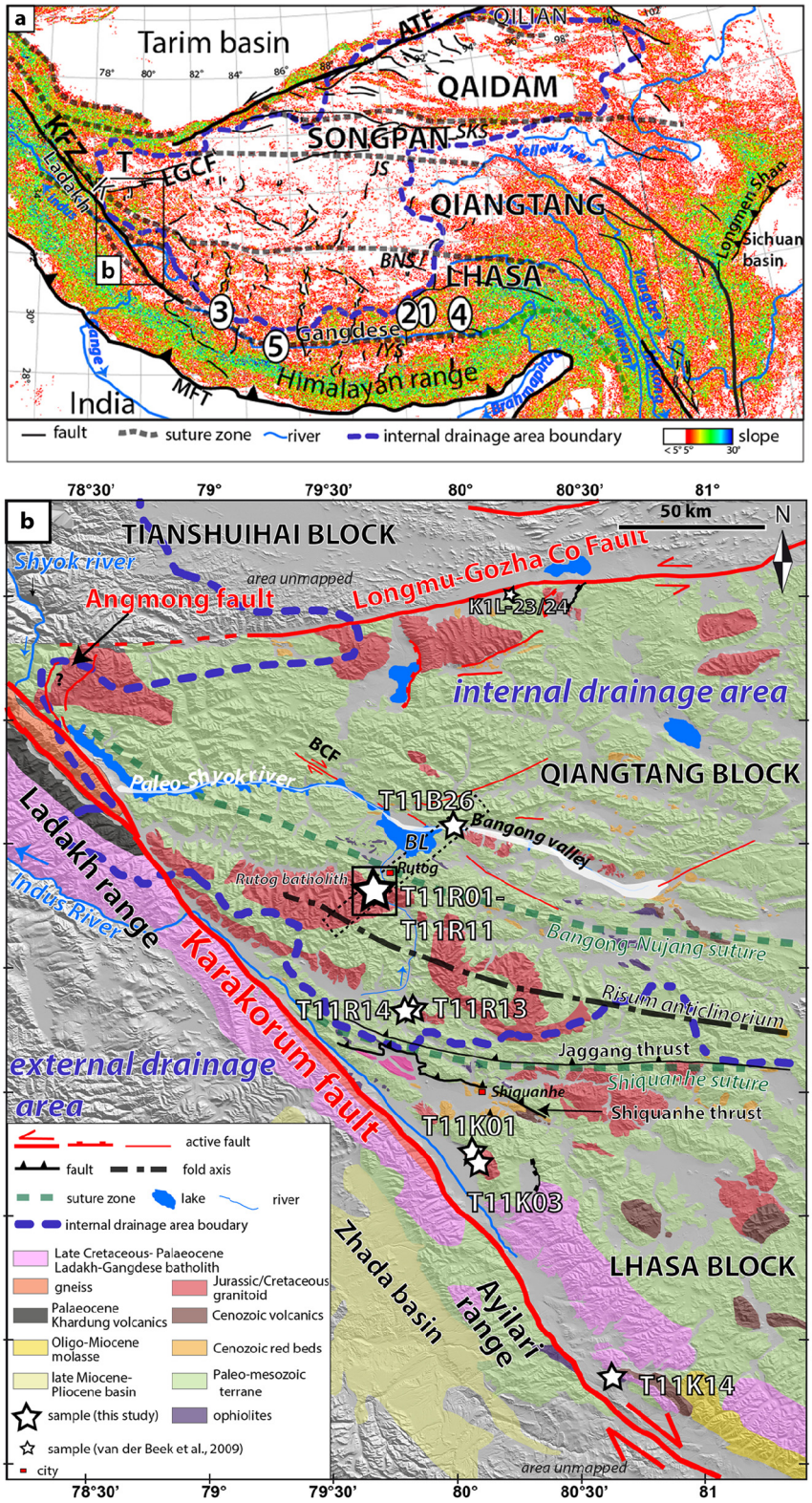

Fig. 1. a) Geologic and geomorphic framework of Tibet. Tectonic features are from Tapponnier and Molnar (1977) and Pan et al. (2004). Slope distribution was calculated using SRTM images with a ~800 m/pixel resolution. The blue dashed line is the boundary of the modern internally drained area (Strobl et al., 2012). Green dashed lines are sutures zones: IYS = Indus–Yarlung; BNS = Bangong–Nujang; JS = Jinsha; SKS = South Kunlun. Black lines are active faults: KFZ = Karakorum Fault Zone; ATF = Altyn Tagh Fault, LGCF = Longmu–Gozha Co fault; MFT = Main Frontal Thrust. K = Karakorum range; T = Tianshuihai block. Numbers refer to articles discussed in section 5.3. 1: Copeland et al. (1995); 2: Dai et al. (2013); 3: Sanchez et al. (2013); Carrapa et al. (2014); 4: Tremblay et al. (2015); 5: Shen et al. (2016). **b)** Regional map of western Tibet. The topography is shown by a shaded relief SRTM (Shuttle Radar Topography Mission) mosaic, which has a 30 m/pixel resolution. Faults and geology are drawn after Pan et al. (2004), Matte et al. (1996), Tapponnier and Molnar (1977), Leloup et al. (2012), Valli et al. (2007), Gourbet et al. (2015) and our own field observations and interpretations from satellite imagery. The purple dashed line differentiates the internally drained area from the Indus and Shyok river drainage basins, and was drawn by ascertaining flow directions of all rivers in the area, using Google Earth. The black square indicates the location of the age-elevation profile. The Paleo-Shyok river that used to flow in the present-day Bangong valley (see section 5.3.2) is highlighted in white. BCF: Bangong Co fault. (For interpretation of the references to color in this figure legend, the reader is referred to the web version of this article.)

have been dated at 21–24 Ma (Arnaud, 1992; Kapp et al., 2003; Williams et al., 2004; Gourbet et al., 2015) indicating that the fault was active after 21 Ma.

3. Sampling and method description

3.1. Sample selection

3.1.1. Rutog area

Both the western Qiangtang and Lhasa blocks include several kilometer-scale granitic plutons, one of which is the Rutog batholith (Fig. 1b). A total of 11 samples were collected for apatite (U–Th–Sm)/He and ^{4}He/^{3}He thermochronology from the Rutog batholith, which is composed of several km-large plutons of granodiorite and granite. 8 samples (T11R01–T11R11) were collected along an age-elevation profile in a N–S trending, narrow valley, 15 km south of the southernmost edge of the Bangong Lake (Fig. 1b). The seven highest elevation samples come from the western flank of the valley, and the lowest comes from the eastern flank. Because the river in this valley flows into the Bangong Lake, we consider them the same geomorphic feature with interrelated histories. Total elevation difference is 700 m and the horizontal distance along the seven highest samples is 1200 m. All samples have the same lithology, *i.e.* a pale granodiorite rich in amphibole and cm-scale K-feldspar (Supplementary Fig. F1a). Amphiboles are chloritized and plagioclase feldspars are slightly altered into sericite. K-feldspars are fresh. Minor phases include zircon and apatite. We did not observe any faults within the pluton. It is locally cut by mm to cm-scale aplitic veins (Supplementary Fig. F1b). On its lowest portion the pluton also contains several dark, centimeter-scale dioritic xenoliths and is cut by a 1-m-wide, strongly weathered basalt dyke (Supplementary Fig. F1c). A ∼4-m-wide vein of microgranite rich in biotite and hornblende cuts both the aplites and the granodiorite pluton. This microgranite was sampled for U/Pb dating (sample T11R08, Supplementary Fig. F1d), in order to constrain the age of pluton crystallization.

Sampling along a horizontal transect can be used to constrain the past topography (House et al., 1998) by taking advantage of isotherms mimicking topography at shallow depths (Mancktelow and Grasemann, 1997). However, we were only able to collect one sample in a granitic biotite-rich pluton (T11B26, ∼4 km NE of the Bangong Lake, Fig. 1b). We use it for comparison with the Rutog age-elevation profile samples.

About 50 km south of the vertical profile site, on the hanging wall of the Shiquanhe thrust, a similar pluton, except for weathered K-feldspars, is surrounded by a metamorphic hornfels aureole. This pluton was also sampled for (U–Th–Sm)/He dating (sample T11R13 and T11R14, Fig. 1b).

3.1.2. Shiquanhe area

3 samples were collected south of the Shiquanhe thrust fault (footwall), near the Indus River (Fig. 1b). Lithologies are diverse. Sample T11K01 is a microgranite and was collected on a high elevation pass. Sample T11K03 and T11K14, collected on the eastern side of the Indus River valley, are unweathered granodiorites that are rich in pink K-feldspar and biotite. Sample T11K14 also contains amphibole. Minor phases include zircon and apatite.

3.2. Methods

3.2.1. U/Pb geochronology of zircon

U/Pb dating was performed by laser ablation inductively coupled plasma mass spectrometry (LA-ICP-MS) at the Laboratoire Magmas et Volcans, Clermont-Ferrand, France. 15 measurements were done *in situ* on 10 zircons selected from a thin section of sample T11R08. The method is fully described in the supplementary section B.

3.2.2. (U–Th–Sm)/He thermochronology of apatite

(U–Th–Sm)/He dating has been widely used for reconstructing exhumation through geological time (e.g. Ehlers and Farley, 2003). For apatite, the closure temperature of that system is about 65° (Shuster et al., 2006, calculated after Dodson, 1973). This value can vary through time as radiation damage modifies He diffusivity in apatite, thus leading to closure temperatures ranging from about 45 to 120 °C (Shuster et al., 2006; Flowers et al., 2009). A partial retention zone spanning between 85–40 °C (Wolf et al., 1998) makes this system useful when examining exhumation processes in the upper 2 km of the crust.

For each sample, at least 3 euhedral apatite crystals containing minimal inclusions were selected for single-crystal (U–Th–Sm)/He measurements (Table 1). All analyses were completed in the Noble Gas Thermochronometry Laboratory at the Berkeley Geochronology Center, California. Detailed information on the analytical procedures can be found in Tremblay et al. (2015).

3.2.3. ^{4}He/^{3}He thermochronology of apatite

To further constrain the cooling history, ^{4}He/^{3}He thermochronometry was conducted on 4 samples. ^{4}He/^{3}He thermochronometry constrains continuous cooling path of individual rock samples below ∼90 °C (Shuster and Farley, 2004). This method is based on a stepwise degassing ^{4}He/^{3}He analysis of a single apatite crystal containing ^{3}He generated by energetic proton irradiation (Shuster et al., 2004), and constrains the spatial distribution of ^{4}He within the grain, which resulted primarily from radiogenic production and thermally controlled diffusive loss through geological time. Combining both (U–Th–Sm)/He ages and ^{4}He/^{3}He thermochronometry allows us to model the continuous thermal evolution of the samples, as explained in paragraph 5.2. This numerical method is fully described in Schildgen et al. (2010) and Tremblay et al. (2015). All ^{4}He/^{3}He measurements were performed in the Noble Gas Thermochronometry Laboratory at the Berkeley Geochronology Center.

4. Results

4.1. U–Pb geochronology of zircon

Zircon U/Pb dating of sample T11R08 yielded 5 concordant analyses at *ca.* 74 Ma (^{206}Pb/^{238}U age, Fig. 3, supplementary Table S1.). Linear regression through 12 spots indicates a lower intercept at 74.4 ± 1.9 Ma (MSWD = 3.9), which is interpreted as the crystallization age. This late dyke age is in agreement with the 80.0 ± 1.2 Ma (sample RT-1) and 79.4 ± 0.9 Ma (sample RT-7) zircon U/Pb ages of the batholith reported by Zhao et al. (2008). These authors suggest that formation of this batholith is best explained by partial melting of a thickened continental crust, in good accordance with the hypothesis of a Late Cretaceous formation of the Shiquanhe suture to the south (Matte et al., 1996).

4.2. (U–Th–Sm)/He thermochronology of apatite

Most single grain apatite (U–Th–Sm)/He (AHe) ages from the Rutog area (T11B26, T11R01 to T11R11, Fig. 1b) range from 11.9 to 29.2 Ma (Table 1 and Fig. 2). Single grain apatite AHe ages of samples T11R14 and T11R13 range from 36.35 to 48.62 Ma. Replicates from sample T11R13 show a high degree of dispersion (standard deviation ∼11 Ma). AHe ages from the age-elevation profile show a clear age-elevation correlation (Fig. 2), and a linear regression through the median ages provides an apparent exhumation rate of ∼70 m/Ma ($r^2 = 0.7$). Apatite fission track ages from two samples from the Rutog batholith of 50.35 ± 9.73 Ma (sample K89G131) and 56.96 ± 5.7 Ma (sample K89G111, precise latitude

Table 1
(U–Th–Sm)/He apatite dating results.

Sample	Grain	Lat. (°)	Long. (°)	Elevation (m)	^{238}U (nmol/g)	^{232}Th (nmol/g)	eU (nmol/g)	^{147}Sm (nmol/g)	^{4}He (nmol/g)	a (μm)	Raw age (Ma)	F_T	Corrected age (Ma)	± (Ma)
Rutog														
T11B26	x	33.572	79.978	4281	36	124	65	490	1.1	55.1	13.22	0.73	**18.22**	0.25
	y				36	127	66	514	1.2	58.4	13.81	0.75	**18.64**	0.24
	z				79	379	168	919	2.8	56.2	12.83	0.74	**17.70**	0.19
T11R01	x	33.315	79.676	5030	104	388	196	164	3.2	52.8	12.79	0.72	**18.20**	0.19
	y				140	516	261	228	5.0	49.7	14.81	0.70	**21.58**	0.98
	z				42	151	78	82	1.6	57.8	16.26	0.74	**22.31**	0.28
T11R02	x	33.316	79.679	4897	106	205	154	100	2.5	46.8	12.67	0.68	**18.85**	0.5
	y				51	65	66	37	1.5	47.3	17.64	0.69	**26.00**	0.33
	z				57	126	87	80	1.6	59.6	14.51	0.75	**19.61**	0.33
	a[a]				27	100	51	26	3.0	54.3	10.92	0.73	**15.37**[c]	1.54
T11R03	x	33.314	79.679	4776	133	533	259	350	4.4	70.9	13.09	0.79	**16.83**	0.17
	y				89	317	163	125	2.4	49.7	11.4	0.70	**16.67**	0.22
	z				83	273	147	109	2.9	45.6	15.24	0.68	**23.13**	0.31
T11R04	bis	33.313	79.681	4652	92	354	176	176	2.4	55.8	10.54	0.71	**15.11**	0.19
	y				85	294	154	115	2.3	55.9	11.62	0.74	**16.11**	0.18
	z				40	128	70	58	0.8	49.8	8.86	0.74	**12.15**	0.17
T11R05	x	33.311	79.683	4516	57	138	90	181	1.2	78.0	10.51	0.81	**13.11**	0.14
	y				46	132	77	70	0.9	50.9	9.32	0.71	**13.41**	0.21
	z				104	286	171	102	2.6	52.4	11.99	0.72	**17.03**	0.22
T11R06	x	33.311	79.686	4409	94	268	157	71	3.9	0.7	19.12	0.67	**29.25**	0.31
	y				71	143	104	58	1.7	51.4	12.32	0.71	**17.59**	0.24
	z				73	128	103	44	1.3	48.1	9.99	0.69	**14.65**	0.22
T11R10	x	33.311	79.688	4361	62	125	91	89	1.1	53.0	9.73	0.72	**13.71**	0.7
	y				70	115	97	84	1.7	62.6	13.28	0.76	**17.58**	0.22
	z				56	147	91	71	1.0	49.6	8.21	0.70	**11.93**	0.15
T11R11	x	33.290	79.695	4346	139	213	190	89	2.3	57.4	9.37	0.74	**13.27**	0.16
	y				203	486	317	216	4.0	60.9	9.9	0.76	**12.77**	0.14
	z				34	42	44	10	2.6	49.3	19.18	0.70	**15.95**	0.18
	b_z				212	361	296	136	3.7	64.8	9.7	0.75	**13.08**	0.14
T11R13	x	32.827	79.808	4600	46	118	74	452	4.2	45.9	42.77	0.68	**36.35**	0.77
	y				28	90	49	336	2.2	51.5	33.31	0.71	**47.10**	0.68
	z				37	95	59	326	2.1	57.1	27.45	0.76	**63.55**	0.67
T11R14	x	32.827	79.808	4606	121	30	128	89	4.2	44.1	32.39	0.67	**48.62**	0.45
Shiquanhe														
T11K01	x	32.320	80.009	4760	421	555	552	916	17.9	56.9	24.95	0.74	**34.02**	0.33
	y				437	1009	674	1095	24.8	66.4	28.44	0.78	**37.04**	0.5
	z				461	901	673	1008	83.3	59.5	95.17	0.75	**128.07**[b]	1.68
T11K03	x	32.268	80.030	4336	164	547	292	551	8.3	58.5	24.44	0.75	**29.98**	1.68
	y				87	252	146	339	4.8	61.4	22	0.76	**33.77**	0.34
	z				30	118	57	76	7.7	55.6	25.26	0.73	**34**	0.45
T11K14	x	31.454	80.561	4747	298	1300	603	200	14.6	44.9	18.86	0.67	**22.11**	0.2
	y				341	61	355	428	9.5	56.3	20.51	0.74	**27.81**	1.14
	z				318	1158	590	106	12.9	69.9	17.11	0.79	**28.98**	0.29

a = radius of a sphere with equivalent volume to surface ratio, calculated from measured cross-dimensions of the analyzed grain.
Underlined samples are from the altitudinal profile.
[a] Indicates one or a few microscopic inclusions.
[b] Replicate excluded from interpretation due to high He content and an assumed Cretaceous age of crystallization of the sample.
[c] Age calculated using ^{4}He/^{3}He degassing steps.
The corrected grain ages are obtained after applying the alpha-ejection factor F_T to the raw ages.
The uncertainties reported in the table are 1 SD analytical uncertainties, which commonly provide a lower bound on the uncertainty of a given (U–Th)/He age, due to other sources of uncertainty that are difficult to estimate, e.g. associated with alpha ejection, radiation damage and its influence on diffusivity, and the possibility of microscopic mineral inclusions that may contain U or Th. Since reproducibility of (U–Th–Sm)/He ages between mineral aliquots of monitor samples (Durango apatite) is typically 6%, we use this fixed value as an estimate of the (U–Th–Sm)/He age uncertainty in our analysis.

and longitude unknown but collected along the same narrow valley) (Arnaud and Vidal, 1990) are older and thus consistent with our data. van der Beek et al. (2009) reported a 17.2 ± 0.6 AHe age from a granitic boulder (K1L-23/24, Fig. 1b) in the Longmu Co range, 140 km north of our samples, south of the GLCF. Samples from the Shiquanhe area (T11K01, T11K03, T11K14) have single grain AHe ages ranging from 22.11 to 37.04 Ma (Table 1).

For all samples, it appears that there is no link between anomalously old ages and the presence of inclusions in some grains, except for one sample (T11R06). T11R06 has poor reproducibility (standard deviation ~16 Ma), due to anomalously high Th content in one of the replicates, likely resulting from an unidentified inclusion. This sample was excluded from thermal modeling.

4.3. ^{4}He/^{3}He thermochronometry

We analyzed four samples of the Rutog age-elevation profile (T11R02, T11R04, T11R05 and T11R10) using ^{4}He/^{3}He thermochronometry. Degassing ^{4}He/^{3}He release spectra are provided in Fig. 4 and supplementary Table S2. When using apatites for cooling history reconstruction purposes, it is often assumed that the ^{4}He/^{3}He spectrum is solely due to diffusion and alpha ejection pro-

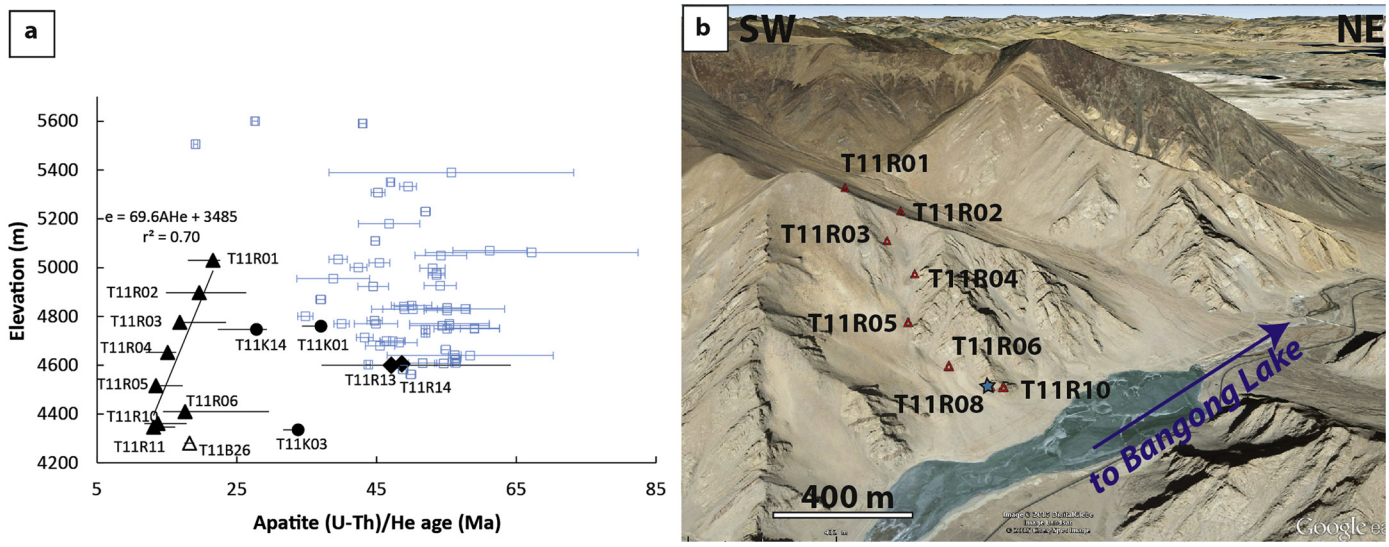

Fig. 2. a) Apatite (U–Th–Sm)/He cooling ages from this study (black symbols) and from central Tibet (blue squares). Full triangles correspond to the 8 granodiorite samples (T11R01–T11R11) from the age-elevation profile. Symbols show the median age for each sample; horizontal lines correspond to the data dispersion. To depict the data dispersion we substracted the age of the youngest replicate from the age of the oldest replicate, for each sample. For example, for sample T11R01 the black horizontal line is calculated as follows: 22.31 (AHe age of grain T11R01z) + 0.28 (uncertainty on this age) – 18.20 (AHe age of grain T11R01x) – 0.19 (uncertainty on this age). For comparison, samples from internally drained central Tibet are plotted after Hetzel et al. (2011) and Rohrmann et al. (2012) (mean AHe ages with a 1σ error), and Haider et al. (2013) (mean AHe ages with a 2σ error). Young cooling ages at ca. 19 and 29 Ma from Rohrmann et al. (2012) are related to local tectonic exhumation. **b)** Google Earth view of the age-elevation profile; T11R11 is not shown because it is located ~1800 m upstream and on the valley floor. (For interpretation of the references to color in this figure legend, the reader is referred to the web version of this article.)

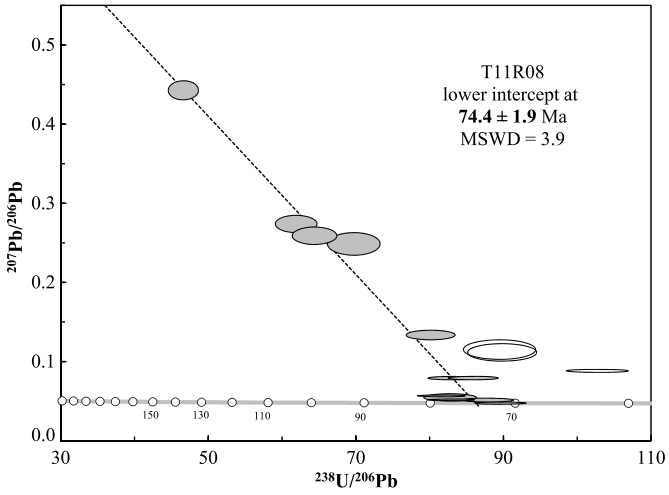

Fig. 3. Tera-Wasserburg diagram for sample T11R08. Empty ellipses correspond to zircons that experienced Pb loss and were not used in the age calculation. Errors are 2σ.

cesses, and that natural ^{4}He was produced homogeneously within the grain. However, Farley et al. (2011) demonstrated that zonation in eU (effective uranium = [U] + 0.235*[Th], which weights these elements by their relative alpha productivity), can significantly affect the shape of the ^{4}He/^{3}He spectrum and subsequent interpretation. Qualitatively, sample T11R02 shows no evidence of zonation because the shape of its spectrum (Fig. 4a) has a similar shape to that of theoretical spectra of unzoned crystals as calculated by Shuster and Farley (2004). The grain used for ^{4}He/^{3}He thermochronometry was also dated using the (U–Th–Sm)/He method by measuring the U and Th content of the same crystal. eU spatial distribution was estimated for samples T11R04 and T11R10 following the method described in Farley et al. (2011) and Tremblay et al. (2015) (supplementary section D). Sample T11R10 presents a clear zonation in eU whereas sample T11R04 shows limited evidence of zonation.

5. Discussion

5.1. A possible inherited topography?

The two lowest-elevation samples from the age-elevation profile with an elevation close to that of T11B26 (4281 m, median AHe age = 18.6 Ma, 40 km NW of the vertical profile) have median AHe ages of 13.3 and 13.7 Ma. The cooling age difference between these samples and T11B26 is about 5 Ma. Samples from the age-elevation profile with cooling ages close to the age of T11B26, such as sample T11R02 (4897 m) and sample T11R03 (4776 m), are ~570–620 m higher than the elevation of T11B26 (Fig. 5). Such age or elevation differences suggest that the elevation of the closure temperature isotherm is at shallower depth beneath the vertical profile than beneath T11B26, i.e. below the Bangong valley. To investigate if this difference could be the effect of an inherited topography, we used the 2D equation of Turcotte and Schubert (2002) to calculate the shape of isotherms (equation (1)), taking into account the effect of heat flow and topography on crustal temperature. This equation allows us to calculate temperature beneath a periodic topography, as a function of depth under the mean elevation (z) and horizontal distance along a transect perpendicular to the ridges and valleys (x). Parameters are given in Table 2.

$$T = T_0 + \frac{q_m z}{k} + \frac{\rho H_s h_r^2}{k}\left(1 - e^{\frac{-z}{h_r}}\right) + \left(\beta - \frac{q_m}{k} - \frac{\rho H_s h_r}{k}\right) h_0 \cos\frac{2\pi x}{\lambda} e^{\frac{-2\pi z}{\lambda}} \quad (1)$$

Although the topography in western Tibet is not periodic *sensu stricto*, it is characterized by roughly parallel valleys at ~4200–4400 m, separated by crests as high as 6000 m. We used a periodic topography that approximately fits the local topography (Fig. 5a): a 60-km-wavelength and an amplitude of 1600 m. Beneath the valley floor (T11B26, Fig. 5b), the 60 °C isotherm is ~600 m deeper than beneath the ridge (at the Rutog age-elevation profile location). If such an elevation difference existed at ~19 Ma (AHe age of T11B26) it may explain why samples at the Rutog age-elevation

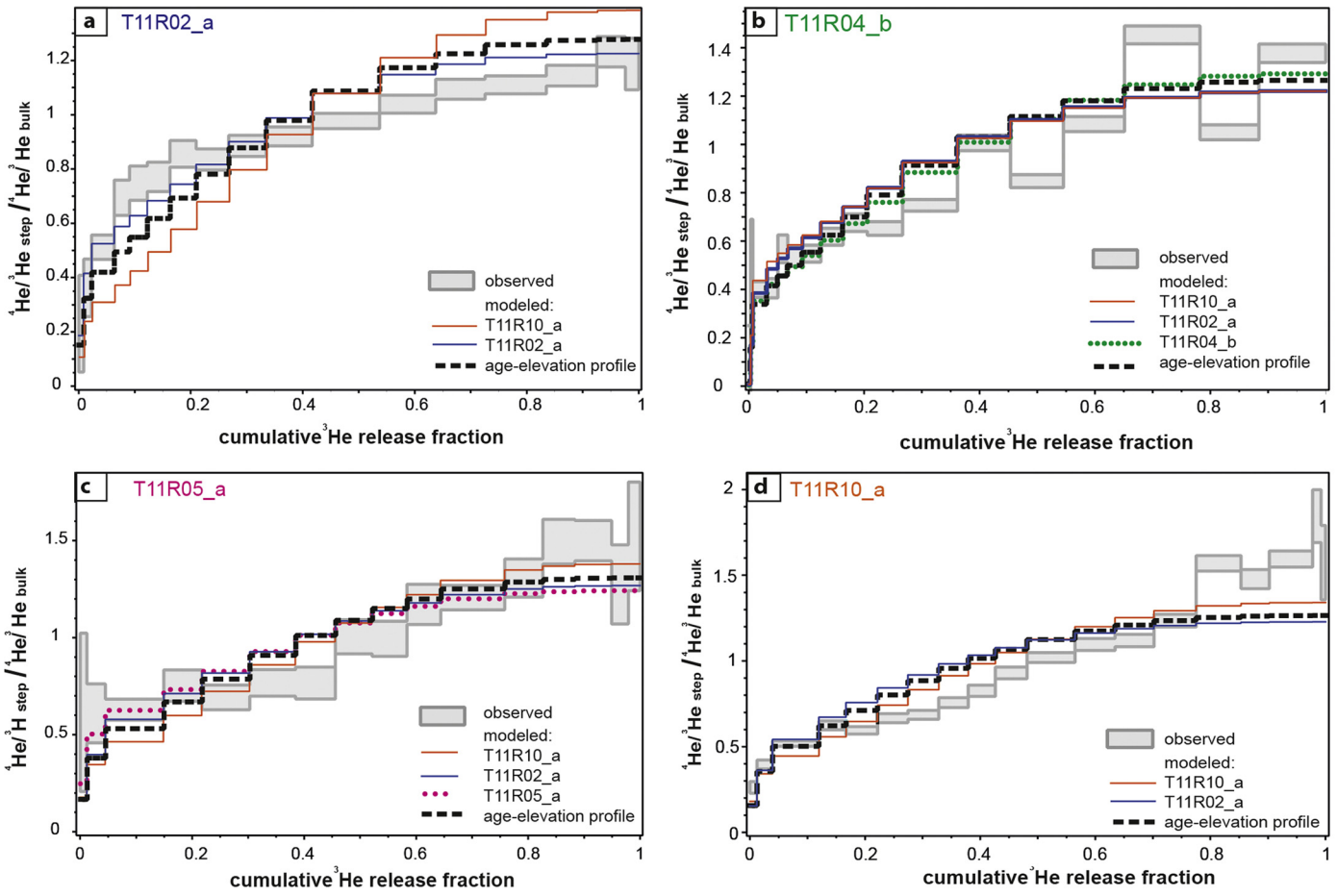

Fig. 4. $^4He/^3He$ ratio evolution diagrams from thermal modeling for individual samples. For all samples, grey boxes are the observed ratios for each step of the experiment. The blue and orange lines are the predicted spectra if the sample follows the same time-temperature paths than T11R02 (high elevation sample) and T11R10 (low elevation sample) respectively (shown on Fig. 6). A black dashed line corresponds to the predicted spectrum of the considered sample when modeling data from the entire age-elevation profile. **a)** Sample T11R02. The blue line is the degassing spectrum corresponding to the best model for sample T11R02. **b)** Sample T11R04. The green dotted line is the predicted spectrum corresponding to the best model for sample T11R04. **c)** Sample T11R05. The pink dotted line is the degassing spectrum corresponding to the best model for sample T11R05. **d)** Sample T11R10. The orange line is the degassing spectrum corresponding to the best model for sample T11R10. (For interpretation of the references to color in this figure legend, the reader is referred to the web version of this article.)

profile that are similar in age to T11B26 are located 570–620 m higher. This calculation suggests that by 19 Ma, topography had the same amplitude, and valleys were located at the same location as today. However, this reconstruction is based on a single valley bottom sample (T11B26), and additional samples would be required to test this hypothesis. Despite this limitation, our hypothesis is consistent with a recent morphological and sedimentary study suggesting that the present day Bangong Valley morphology is mostly inherited from a topography formed 24 Ma or 37 Ma ago (Gourbet et al., 2015).

5.2. Evolution of erosion rates in western Tibet

5.2.1. Rutog batholith age-elevation transect first-order interpretation

A linear regression through the median ages gives an apparent exhumation rate of ca. 70 m/Ma between 23 and 12 Ma (Fig. 2). This is an oversimplification because it is based on the assumptions that all samples have the same closure temperature, corresponding isotherms remained horizontal through time with no heat advection or post-magmatic cooling, and that the profile is purely vertical and the area was not tilted. Given the age difference between the AHe ages and the last documented plutonic event at about 74 Ma, post intrusion cooling is unlikely. Because the general wavelength of the topography in this area is about 60 km, i.e. 20 times greater than the maximum horizontal distance between the samples, the wavelength of the topography should not affect these samples. The valley is 700 m-wide; at short wavelengths (<8 km), the topography does not significantly deflect low-temperature isotherms in the crust (Braun, 2002). Therefore, we can use the order-of-magnitude of the apparent exhumation rate as a proxy for the erosion rate, which indicates that erosion rates were already low in western Tibet during Miocene time. This value of 70 m/Ma is similar to the Holocene erosion rates from 110 to 40 m/Ma estimated in central Tibet based on exposure dating (Lal et al., 2003; Hetzel et al., 2011; Strobl et al., 2012). Climatic conditions are similar in central and western Tibet, with western Tibet being slightly drier (Yatagai et al., 2012), suggesting that erosion rate in western Tibet has the same order-of-magnitude as in central Tibet. Thus, the apparent Miocene exhumation rate interpreted from the AHe data has the same order-of-magnitude as the probable modern erosion rate in western Tibet.

5.2.2. 1D thermal history modeling

The age-elevation profile can reflect cooling histories that are more complex than a single phase of exhumation. Combining both $^4He/^3He$ and (U–Th–Sm)/He data allows us to better reconstruct the local exhumation history. $^4He/^3He$ profiles provide additional constraints on the cooling history from ~90 °C to the surface (Shuster and Farley, 2004). To integrate both $^4He/^3He$ and (U–Th–

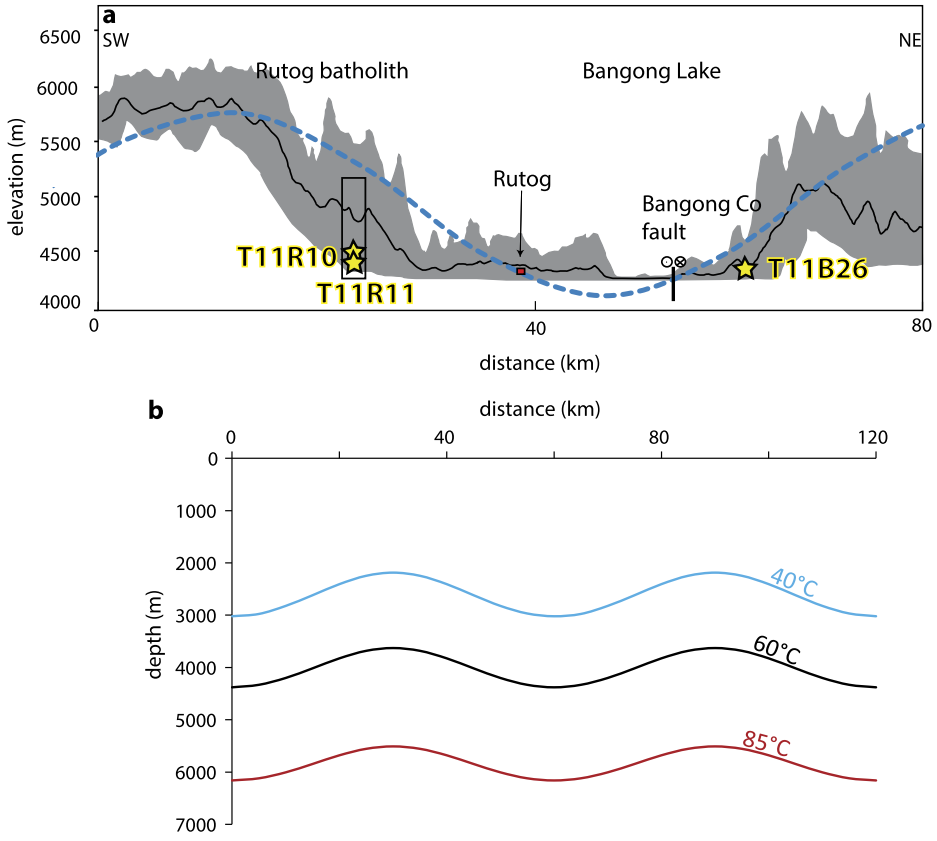

Fig. 5. a) Local elevation profile perpendicular to the main Bangong valley. The black line is the mean elevation and the grey envelope shows all elevation values. The blue dotted line is a theoretical periodic topography of 60 km wavelength and 1800 m amplitude. **b)** Depths of crustal isotherms assuming the periodic topography shown on a) and calculated using equation (1). (For interpretation of the references to color in this figure legend, the reader is referred to the web version of this article.)

Table 2
Parameters used in equation (1) to approximate the crustal temperature beneath a periodic topography.

Parameter	Dimension	Value	Reference
β	Lapse rate of surface temperature, °C/m	0.006	Turcotte and Schubert (2002)
T_s	Mean surface temperature, °C	0	
K	Thermal conductivity, W/K/m	2.5	Turcotte and Schubert (2002)
q_m	Reduced heat flow (mantle), W/m	0.025	Turcotte and Schubert (2002)
h_r	Characteristic depth of heat production, m	1000	Turcotte and Schubert (2002)
h_0	Relief 1/2 amplitude, m	800	
λ	Relief wavelength, m	6E+04	
ρH_s	Crustal radioactive heat production, W/m^3	1.5E−6	Craig et al. (2012)

Sm)/He data, we used the 1D QTQt program (Gallagher, 2012), in order to infer thermal histories from the Rutog pluton. This program calculates the most probable cooling path of a single sample, as well as multiple samples from an age-elevation profile. It requires an assumed geothermal gradient. Estimates from central Tibet are 25 °C/km (Qiangtang block) and 39 °C/km (Lhasa block) (Mechie et al., 2004), and 17 °C/km in the northern Qiangtang block since 3 Ma (Hacker et al., 2000). Although we recognize that this is an assumption based on present conditions applied to the Miocene, we used a value of 30 °C/km. The reader is referred to the supplementary section (Appendix B) for detailed information on QTQt.

First, we modeled samples T11R02, T11R04, T11R05 and T11R10 individually (Fig. 6). For each sample, we used both AHe ages and ^{4}He/^{3}He data. All models imply a three-phase cooling history: 1) an early slow cooling phase, 2) an increase in the cooling rate, and 3) a final slow cooling phase. Additionally, sample T11R10 shows a slight reheating from 20 to 10 Ma. This might be due to the location of the sample. Indeed, T11R10 was collected ∼5 m from the 1-m-thick basaltic dyke described in section 3.1.1. The

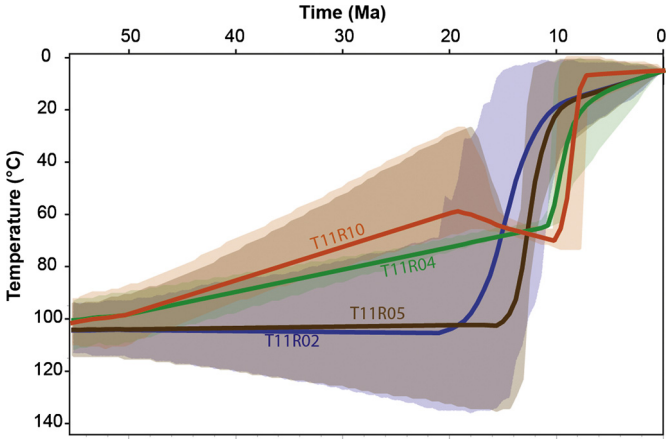

Fig. 6. Individual cooling histories modeled with QTQt. Envelopes delimit the 95% confidence intervals.

dyke might have caused the apparent reheating experienced by sample T11R10, but the duration of the reheating (10 Ma) does not match the timescale of heating events due to volcanism, which are usually much shorter (Reiners, 2005). In addition, samples that are higher in elevation do not seem to record any reheating event and clearly show a decrease in temperature. Although we cannot rule out the thermal effect of this narrow dyke, it is unlikely that it caused a wide portion of the pluton to reheat during 10 Ma. The main differences between the models for each sample are the timing and amplitude of the second, rapid cooling step: the samples appear to record different rates of rapid cooling, ranging from 8.5 °C/Ma to 20 °C/Ma, and the timing varies from 20 to 8 Ma (Fig. 6).

Because the confidence envelopes overlap, the discrepancy between these 4 models could be due to insufficient resolution of our data. We tested this hypothesis by conducting additional modeling presented in the supplementary section C and Fig. 4. These tests show that when modeled individually, the samples do not seem to record the same cooling history and the data resolution is not the cause for the discrepancies described above. In summary, all thermal histories inferred from individual samples seem to point to a 3-phase history, characterized by an acceleration of the cooling during the middle Miocene, but the timing and amplitude of this acceleration cannot be accurately resolved using solely modeling of individual samples. To determine if the models can be reconciled with a thermal history that reflects the evolution of the whole Rutog pluton, we used QTQt to model the dataset from the age-elevation transect (Fig. 7a). Because the precise elevation and elevation of the samples from Arnaud and Vidal (1990) are not known, we did not include his apatite fission tracks ages in the model.

The resultant model reproduces both the ^{4}He/^{3}He data (Fig. 4) and the observed ages (Fig. 7b). As in the case of sample T11R02, the model also implies very slow cooling prior to 20 Ma. Apatite fission track ages of ~50 Ma and ~57 Ma (Arnaud and Vidal, 1990) are consistent with this slow cooling phase that could have started in early Eocene. This was followed by two pulses of rapid cooling, from 19 to 17 Ma and ~11–9 Ma. Given the discrepancies in cooling histories inferred from individual ^{4}He/^{3}He spectra, one could argue that these two rapid cooling phases may actually be one single phase, starting at *ca.* 20 Ma and ending at 9 Ma. We tested this hypothesis using additional modeling presented in supplementary section C. Based on these models, we are confident that our preferred cooling path is the most appropriate to explain all of the observations and experimental data that we present here. Finally, after the last cooling pulse ended at 9 Ma, the cooling appears to be very slow.

Using a mean geothermal gradient of $30 \pm 10°$/km, converting the two cooling pulses into exhumation rates gives $\sim 420^{+210}_{-105}$ m/Ma (from 19 to 17 Ma) and $\sim 840^{+430}_{-210}$ m/Ma (from ~11 to 9 Ma). Since there is no field evidence of local tectonic denudation, exhumation in the Rutog area is likely solely due to erosion. Based on the models, the total erosion during the two pulses would be about 1500 m. Although the AHe age of 17.2 in the Longmu Co range (van der Beek et al., 2009) falls in the range of our AHe ages, we do not have sufficient data to assess whether the Rutog and Longmu Co areas experienced comparable low temperature cooling histories.

5.3. Control of exhumation and geomorphic evolution of western Tibet

Previous studies of the central Tibetan plateau suggest that following India–Asia collision, the plateau experienced continuous slow cooling and erosion (van der Beek et al., 2009; Hetzel et al., 2011; Rohrmann et al., 2012; Haider et al., 2013) consistent with an internally drained plateau. In western Tibet, except

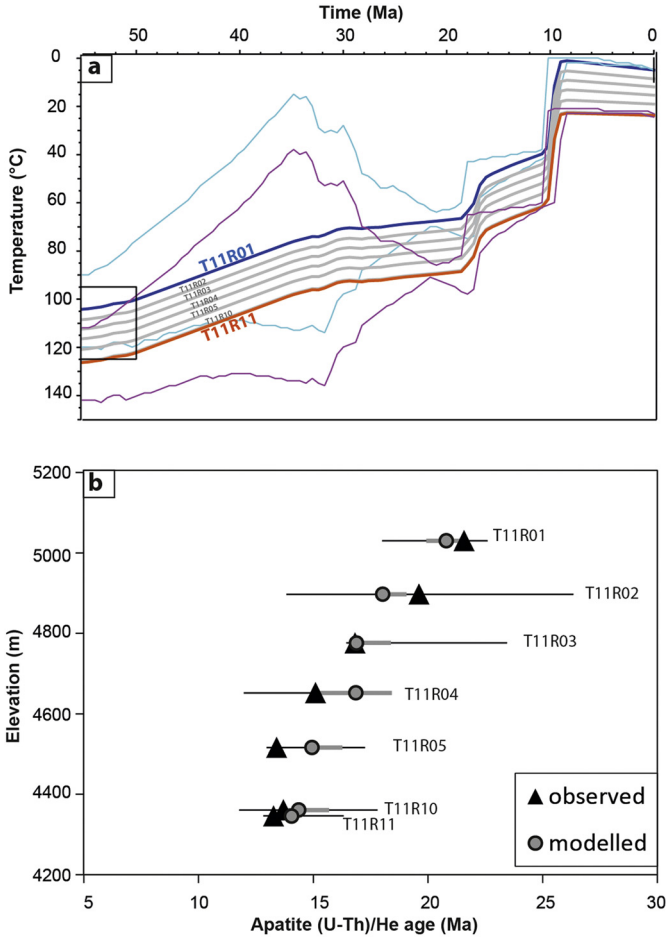

Fig. 7. a) Time-temperature paths of 7 samples from the Rutog age-elevation profile, modeled with QTQt, with input of AHe ages and ^{4}He/^{3}He data. The orange Tt path corresponds to the lowest sample (T11R11) and the dark blue Tt path to the highest sample (T11R01). The pink and light blue curves form the 95 % confidence intervals for the orange and light blue Tt paths, respectively. The intervening grey Tt paths correspond to intermediate samples. The black rectangle corresponds to the initial Tt constraint input in the model. **b)** Fit of the modeled ages with the age-elevation relationship. Black and grey lines indicate the dispersion associated with the observed and modeled AHe ages, respectively. (For interpretation of the references to color in this figure legend, the reader is referred to the web version of this article.)

for the 19–17 Ma and 10–9 Ma events, the cooling rate is also very slow and similar to the ones reconstructed in central Tibet. Indeed, samples from the Shiquanhe area (T11K) have similar AHe age-elevation relationships to those found in central Tibet, as do the two samples located north of the Shiquanhe thrust (T11R13–T11R14) whilst these two last samples have a low reproducibility (Fig. 2a, Table 1). The other samples (Bangong area) are slightly younger for a similar elevation (Fig. 2a). This suggests that most of the exhumation history of western Tibet is similar to that of central Tibet except for two short episodes of fast cooling and exhumation. These episodes may be regionally or a locally controlled.

5.3.1. Regional control of the exhumation in western Tibet

Gourbet et al. (2015) hypothesize that western Tibet was connected to the Indus drainage network during Miocene time, before the damming of the Bangong Lake that was caused by the right-lateral motion along the Karakorum fault. This connection made western Tibet sensitive to external parameters, such as regional climate and geodynamics. Therefore, we compare our results with thermochronology studies focusing on externally drained southern Tibet instead of internally drained central Tibet. In particu-

lar, in the Kailas area, Sanchez et al. (2013) and Carrapa et al. (2014) show that rapid exhumation occurred between 19 and 15 Ma and between 18 and 15 Ma, respectively (3 on Fig. 1a). Shen et al. (2016) also document a regional exhumation event at 18–15 Ma in the Gyirong area (5 on Fig. 1a). Near Lhasa (1 and 2 on Fig. 1a), the Gangdese batholith experienced several phases of rapid exhumation between 20 and 8 Ma (Copeland et al., 1995; Dai et al., 2013). Further SE, Tremblay et al. (2015) use AHe and apatite $^{4}He/^{3}He$ thermochronology to show that a rapid cooling phase occurred in middle Miocene time (4 on Fig. 1a). Although the mechanisms regarding the change in exhumation rate differ between these studies and the timing does not necessarily match exactly our observations in western Tibet, most cases show pulses of rapid exhumation between 20 and 8 Ma.

First, regional climate, e.g. the evolution of the Asian monsoon system, is a potential external control for changes in the exhumation rate and, by inference, the incision rate in western Tibet. The increase in the incision rate could be related to an increase in the precipitation during the Miocene. However, knowledge of the Tibetan climate at that time is poor, and global climate models focusing on the Asian monsoon evolution rather suggest a decrease in the precipitation for the western plateau at that time (Ramstein et al., 1997). Global atmosphere circulation simulations from Fluteau et al. (1999) also show low precipitation in western Tibet at 30 and 10 Ma. DeCelles et al. (2007) show evidence of arid climate conditions in central Tibet (N Lhasa block) during the late Oligocene. In the late Miocene–Pliocene Zhada basin of the NW Himalaya (200 km south of the Bangong Lake, Fig. 1b), Saylor et al. (2010) show that sediments deposited in a lake that expanded and regressed following Milankovitch forcing, suggest that global climate controlled the environmental evolution. Saylor et al.'s (2010) findings are compatible with a monsoon, or at least a seasonal climate in SW Tibet. However, the Zhada basin and our study area are presently separated by the Ayilari range that includes peaks higher than 6000 m. As a consequence, western Tibet receives less precipitation than the Zhada area. In any case, our study area was probably protected from precipitation by the early Himalayan range. Thus, although we do not definitively know how sensitive western Tibet was to the monsoon during the Miocene, its influence on the plateau was probably limited.

Second, western Tibet exhumation may be related to regional geodynamics. In particular, the 19–17 Ma increase of the exhumation is contemporaneous with the emplacement of potassic and ultrapotassic magmas in southern Tibet, including the studied area (e.g. Turner et al., 1996; Miller et al., 1999, 2000; Williams et al., 2004; Chung et al., 2005) (Fig. 1b). This magmatic event has been associated with various geodynamic settings, including subduction of the Indian continental margin (Ding et al., 2003), delamination of the Tibetan plateau lithospheric mantle (e.g. Chung et al., 2005) or breakoff of the subducting Indian plate (e.g. Mahéo et al., 2002, 2009). Among these models, delamination may induce uplift and potential exhumation of the studied area induced by isostatic rebound (Houseman et al., 1981). Slab breakoff may also induce uplift following the thickening of the Tibetan crust caused by the underplating of the Indian continental crust (Mahéo et al., 2009). Heating of the Tibetan crust by magma injection and/or the thermal anomaly associated with mantle partial melting may induce uplift of the southern margin of the Tibetan plateau. The abundance of potassic volcanic rocks dated at 24–16 Ma in western Tibet (Arnaud, 1992; Kapp et al., 2003; Williams et al., 2004; Gourbet et al., 2015) clearly implies that a significant thermal perturbation affected the mantle in this area. Additionally, geodynamic changes, such as slab breakoff or delamination, may result in the modification of the dynamic topography (i.e. the part of topography that is due to sublithospheric mantle flow) that affects the Earth's surface at scales ranging from 10 to >1000 km and can be transient over a few Ma to 10 Ma (see review from Flament et al., 2013). These wavelengths and timescales are similar to the area (from western to central Tibet) and duration (1.5–10 Ma) of the rapid exhumation pulses affecting western and central Tibet (this study and references therein). Therefore, dynamic topography is a potential mechanism that could explain the exhumation pattern inferred from our data. In particular, Husson et al. (2014) reconstructed the dynamic component of topography during the Neogene, based on mantle flow above the Indian subducting slab during slab breakoff. The predicted relative surface uplift from 25 to 15 Ma in the Himalaya and Lhasa block is ~1000 m (Husson et al., 2014), and can thus explain the first exhumation episode recorded in western Tibet.

Therefore, the short and moderate 19–17 Ma exhumation pulse recorded in the Rutog area might be related to the geodynamic process that is responsible for the volcanic activity that occurred from ~24 to 16 Ma. However, there is no evidence for a significant regional event that can be correlated with the main exhumation event at about 10–9 Ma, which indicates a more local effect should be considered.

5.3.2. Local control of exhumation in western Tibet

Local tectonics could be responsible for the moderate cooling phases that appear to punctuate an otherwise slow cooling history. Few fault have kinematics (sense and age) that could have played a role in the exhumation of the Rutog batholith.

NW of the Bangong Lake, based on geomorphic features Van Buer et al. (2015) propose the existence of two NS oriented, E dipping normal faults, called the Angmong fault system. Although Van Buer et al. (2015) do not show structural evidence of a normal fault in the Angmong area, an age of 13.7 ± 0.2 Ma in a deformed leucocratic dyke (LB12-48, 35 km west of the West Angmong fault) yields them to propose that normal faulting linked with lower crustal flow lasted until at least that age. It appears however that this sample is located along a ductile strand of the KFZ where dykes of similar age have been described (e.g., Boutonnet et al., 2012) and that this age relates more to the kinematics of the KFZ rather that of the Angmong fault system. In any case, because our samples are located ≥140 km east of the proposed Angmong fault, and would be in the hanging wall, this fault should not affect their exhumation history. The Bangong Co fault is located about 40 km north of the age-elevation profile. It is an active WNW-ESE dextral strike-slip fault, as evidenced by m-scale offset of riverbeds north of the Bangong Lake. Although the precise activation age of the fault is unknown, according to Cheng and Xu (1987) Cenozoic detrital sediments (red beds) are offset by the fault. Thus, it is possible that the Bangong Co fault was active during the Miocene. However, the fault geometry and the associated geomorphology suggest purely strike-slip motion and there is no evidence of local uplift that may be induced by transpressive tectonics. Kinematics of the BCF cannot account for the Rutog batholith exhumation. The Jaggang (Kapp et al., 2003) and the Shiquanhe (Matte et al., 1996) north-dipping thrusts stand south of the Risum anticlinorium and have both been considered as responsible for its uplift. The Jaggang thrust is considered to be Late Cretaceous–early Cenozoic (Kapp et al., 2003). The Shiquanhe thrust was active after 21 Ma (Kapp et al., 2003; Gourbet et al., 2015) and might explain the first rapid cooling event. If the Shiquanhe thrust propagated 50 km north of where it reaches the surface, thrusting could induce formation of local relief north of the fault trace, which would increase local river incision rate and, consequently, the apparent cooling rate. This is consistent with the older AHe ages from 3 samples located in the footwall of the fault; the median ages of samples T11K01, T11K03 and T11K14 range from 27 to 35 Ma (Fig. 2a). However, low reproducibility samples T11R13 and T11R14, also located in

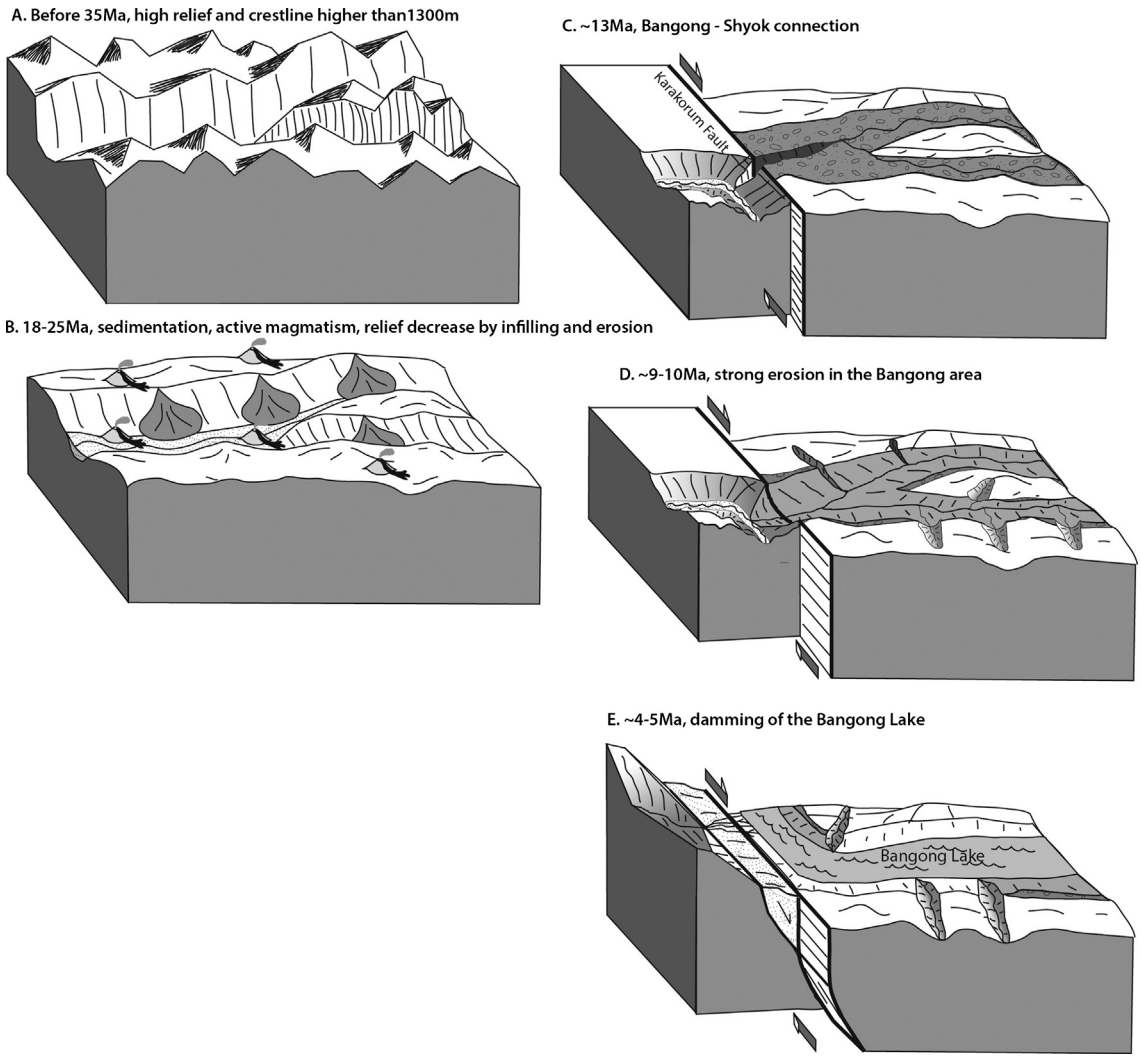

Fig. 8. Landscape evolution of western Tibet at prior to 35 Ma to prior to 24 Ma (A), 18–25 Ma (B), 13 Ma (C), 9–10 Ma (D) and 4–5 Ma (E).

the hangingwall (Fig. 1b), have much older ages than those of the vertical profile and are even older than the samples in the footwall (Fig. 3a). Furthermore, the Shiquanhe thrust seems to have a limited lateral extent ($\leq$100 km) and its throw is about 7 km (Kapp et al., 2003). This implies that motion on that fault is unlikely to have triggered the exhumation of rocks located 50 km away.

Another possible explanation of the ~11–9 Ma event is the reorganization of the river network. Morphologic and sedimentary reconstruction of western Tibet by Gourbet et al. (2015) implies two shifts from an internally to externally drained system since Oligocene time. They demonstrated that some of the modern relief features (2–8 km wide, up to 120 km long valleys) were inherited and that a relief of at least 1.3 km existed during late Oligocene time (Fig. 8A) that was partly filled by detritus (red beds) during the Miocene (Fig. 8B). Such a history is similar to the one proposed for central Tibet (Liu-Zeng et al., 2008) where the decrease in relief by valley filling results from internal drainage (Liu-Zeng et al., 2008). However, the present day geology of western Tibet shows that the detritus that once filled the Oligocene valleys was partly removed from the plateau, which requires external drainage. Ultimately, western Tibet shifted again to a mostly internally drained system, as in present time, despite outburst floods of the Bangong Lake during Holocene time (Dortch et al., 2011).

Gourbet et al. (2015) suggest that major river network reorganization is related to the strike-slip motion along the Karakorum fault. This fault system has been active since at least 14–16 Ma (Wang et al., 2012 and references therein) or prior to 23 Ma (Leloup et al., 2013 and references therein). It offsets the Indus River by about 120 km and its total offset may reach 280–300 km (see Valli et al., 2008 and Leloup et al., 2013 for reviews). Based on a mean slip rate of the Karakorum fault of 11 mm/yr assuming an onset at ~23 Ma (e.g. Lacassin et al., 2004; Valli et al., 2008; Boutonnet et al., 2012; Leloup et al., 2013), river offsets and location and timing of slip along the two main Karakorum fault branches, Gourbet et al. (2015) propose a detailed reconstruction of the river network offset by the Karakorum fault since its initiation. This reconstruction suggests that the Bangong valley became connected to the Shyok river (a major Indus tributary) ~13 Ma ago, thus constituting a paleo-upper Shyok. This configuration (Fig. 8C) corresponds to an offset of 130 km along the Karakorum fault. This would have increased the total length of the Paleo-Shyok channel of 200 km. In addition, the present day Bangong Lake is about 800 m and 100 m higher in elevation than the Shyok and Indus rivers respectively, west of the Karakorum fault. The 200-km length gain would have increased the drainage area and, combined with the modification of the elevation distribution of the drainage area, led to a disequilibrium state of the Paleo-Shyok. This configuration corresponds to the theoretical scenario depicted by Willett et al. (2014) where an instantaneous increase of the upstream area leads to an increase of the average erosion rate. Here, a transient increase of the erosion rate due to the connection between the Bangong valley and the

Shyok river would explain the 840 m/Ma exhumation rate from ∼11 to 9 Ma, especially if the Bangong valley was previously filled by detrital red beds as proposed by Gourbet et al. (2015). The discrepancy between the reconstructed timing of Shyok–Bangong connection at ∼13 Ma and the recorded timing of increased erosion at ∼9–10 Ma could be related to (1) uncertainties in the offset reconstruction, especially in the assumed slip rate of the Karakorum fault that may have varied through time and/or (2) propagation of erosion from the area proximal to the Karakorum fault to the Rutog area, in which the age-elevation profile is located (∼100 km).

Finally, the last stage of the exhumation history is the transition to a low exhumation rate regime, persistent from 9 Ma until today. A possible reason for this transition would be the timelag necessary for the Paleo-Shyok river channel to reach an equilibrium state. Then, the persistence of a negligible exhumation was caused by the transition from an external to an internal drainage; indeed, the connection between the Bangong valley and the lower Shyok ended ∼4 Ma ago (Gourbet et al., 2015), leading to the damming of the Bangong Lake. Given the time resolution of our thermal models, a hypothesis to explain both the decrease of the exhumation at ∼9 Ma and the persistent very low exhumation that followed would be that the abrupt decrease of the exhumation rate is directly related to the separation between the lower Shyok and the Bangong valley due to the continuous motion of the Karakorum fault.

In summary, the most likely scenario is that during a first stage, the Bangong valley was connected to the sea and deep valleys formed (Fig. 8A). Later, this topography was filled with detritus, probably in an internally drained environment (Fig. 8B). Dating of the volcanics that are interbedded with these sediments imply that sedimentation was ongoing around 24–20 Ma (Fig. 8C). Then, due to the strike-slip motion of the Karakorum fault, the Bangong valley connected with the Shyok/Indus system at about 13 Ma (Fig. 8C). This major river network reorganization triggered the evacuation of the Bangong valley sedimentary fill and incision of tributaries such as in the Rutog valley, in which samples from the age-elevation profile were collected (Fig. 8D). This event was relatively short and is followed by a still ongoing slow cooling phase due to equilibration between the Bangong and Shyok rivers and/or separation between both rivers due to Karakorum fault strike-slip and normal motion. (Fig. 8E).

6. Conclusion

Apatite (U–Th–Sm)/He and $^{4}He/^{3}He$ thermochronometry in the Rutog area (Rutog batholith), between the Karakorum dextral strike-slip fault and the sinistral Longmu–Gozha Co strike slip fault indicate that western Tibet experienced slow exhumation rates since the Oligocene, except during two moderate exhumation pulses occurring from 19 to 17 Ma and ∼11–9 Ma, leading to a total incision of about 1500 m. We attribute the first pulse of rapid exhumation to the geodynamic processes responsible for the early Miocene potassic and ultrapotassic volcanic activity occurring in this region. The latest pulse is related to a river network reorganization due the strike-slip motion of the Karakorum fault that connected the Bangong valley to the paleo-Shyok river, leading to an externally drained system and a transient acceleration of the erosion. The exhumation has been negligible since 9 Ma, partly because western Tibet has been mostly internally drained since 4 Ma, due to the damming of the Bangong Lake. Finally, this case study shows the importance of river network distribution on the control of exhumation. Not only does the river distribution control whether or not geodynamic change can be imprinted on the thermochronological record, but it can also directly affect the exhumation rate.

Acknowledgements

We thank Kerry Gallagher for his help with QTQt and Nick Fylstra for his assistance in the Noble Gas Thermochronometry lab. Liu Xiaobing and Liu Xiaohan are acknowledged for their assistance for organizing fieldwork, François Senebier for his technical assistance at ISTerre (Grenoble) and Nicolas Arnaud for helping us with the Ar data. M. Murphy and an anonymous reviewer helped improving this manuscript. This study was supported by the Explora'doc program of the Région Rhône-Alpes, the SYSTER (INSU) and the Cai Yuanpei No. 531 27968UC (French Ministry of Foreign Affairs) programs.

Appendix A. Supplementary material

Supplementary material related to this article can be found online at http://dx.doi.org/10.1016/j.epsl.2016.09.037.

References

Armijo, R., Tapponnier, P., Tong-Lin, H., 1989. Late Cenozoic right-lateral strike-slip faulting in southern Tibet. J. Geophys. Res. 94 (88), 2787–2838.

Arnaud, N., Vidal, P., 1990. Geochronology and geochemistry of the magmatic rocks from the Kunlun-Karakorum geotraverse. In: Colloque Kunlun-Karakorum. IPG, Paris, p. 52.

Arnaud, N., 1992. Apport de la thermochronologie $^{40}Ar/^{39}Ar$ sur feldspath potassique à la connaissance de la tectonique Cénozoïque d'Asie : étude des mécanismes d'accomodation de la collision continentale. PhD thesis. Université de Clermont-Ferrand 2.

Boutonnet, E., Leloup, P.H., Paquette, J.-L., Davis, W.J., Hattori, K., 2012. Synkinematic magmatism, heterogeneous deformation, and progressive strain localization in a strike-slip shear zone: the case of the right-lateral Karakorum fault. Tectonics 31, TC4012. http://dx.doi.org/10.1029/2011TC003049.

Braun, J., 2002. Estimating exhumation rate and relief evolution by spectral analysis of age–elevation datasets. Terra Nova 14, 210–214.

Carrapa, B., Orme, D., DeCelles, P.G., Kapp, P., Cosca, M., Waldrip, R., 2014. Miocene burial and exhumation of the India–Asia collision zone in southern Tibet: response to slab dynamics and erosion. Geology 42 (5), 443–446. http://dx.doi.org/10.1130/G35350.1.

Cheng, J., Xu, G., 1987. Geologic Map of the Ritu Region with Report. Tibetan Bureau of Geology and Mineral Resources, Chengdu, People's Republic of China, 598 p., scale 1:1000,000.

Chevalier, M.L., Li, H., Pan, J., Sun, Z., Liu, D., Wu, C., Pei, J., Xu, W., Huang, X., 2015. First tectonic-geomorphology study along the Longmu–Gozha Co fault system, Western Tibet. Gondwana Res. http://dx.doi.org/10.1016/j.gr.2015.03.008.

Chung, S.-L., Chu, M.-F., Zhang, Y., Xie, Y., Lo, C.-H., Lee, T.-Y., Wang, Y., 2005. Tibetan tectonic evolution inferred from spatial and temporal variations in postcollisional magmatism. Earth-Sci. Rev. 68 (3–4), 173–196. http://dx.doi.org/10.1016/j.earscirev.2004.05.

Copeland, P., Harrison, T.M., Yun, P., Kidd, W.S.F., Roden, M., Zhang, Y., 1995. Thermal evolution of the Gangdese batholith, southern Tibet: a history of episodic unroofing. Tectonics 14, 223–236.

Craig, T.J., Copley, A., Jackson, J., 2012. Thermal and tectonic consequences of India underthrusting Tibet. Earth Planet. Sci. Lett. 353–354, 231–239. http://dx.doi.org/10.1016/j.epsl.2012.07.010.

Dai, J., Wang, C., Hourigan, J., Li, Z., Zhuang, G., 2013. Exhumation history of the Gangdese Batholith, Southern Tibetan Plateau: evidence from apatite and zircon (U–Th)/He thermochronology. J. Geol. 121, 155–172.

DeCelles, P.G., Quade, J., Kapp, P., Fan, M., Dettman, D.L., Ding, L., 2007. High and dry in central Tibet during the Late Oligocene. Earth Planet. Sci. Lett. 253 (3–4), 389–401. http://dx.doi.org/10.1016/j.epsl.2006.11.001.

Ding, L., Kapp, P., Zhong, D.L., Deng, W.M., 2003. Cenozoic volcanism in Tibet: evidence for a transition from oceanic to continental subduction. J. Petrol. 44, 1833–1865.

Dodson, M.H., 1973. Closure temperatures in cooling geological and petrological systems. Contrib. Mineral. Petrol. 40, 259–274.

Domroes, M., Peng, G., 1988. The Climate of China. Springer-Verlag, Berlin, 361 pp.

Dortch, J.M., Owen, L.A., Caffee, M.W., Kamp, U., 2011. Catastrophic partial drainage of the Pangong Tso, northern India and Tibet. Geomorphology 125, 109–121.

Ehlers, T.A., Farley, K.A., 2003. Apatite (U–Th)/He thermochronometry: methods and applications to problems in tectonic and surface processes. Earth Planet. Sci. Lett. 206, 1–14.

Farley, K.A., Shuster, D.L., Ketcham, R.A., 2011. U and Th zonation in apatite observed by laser ablation ICPMS, and implications for the (U–Th)/He system. Geochim. Cosmochim. Acta 75 (16), 4515–4530. http://dx.doi.org/10.1016/j.gca.2011.05.020.

Fielding, E., Isacks, B., Barazangi, M., Duncan, C., 1994. How flat is Tibet? Geology 22, 163–167.

Flament, N., Gurnis, M., Muller, R.D., 2013. A review of observations and models of dynamic topography. Lithosphere 5 (2), 189–210. http://dx.doi.org/10.1130/L245.1.

Flowers, R.M., Ketcham, R., Shuster, D.L., Farley, K.A., 2009. Apatite (U–Th)/He thermochronometry using a radiation damage accumulation and annealing model. Geochim. Cosmochim. Acta 73 (8), 2347–2365. http://dx.doi.org/10.1016/j.gca.2009.01.015.

Fluteau, F., Ramstein, G., Besse, J., 1999. Simulating the evolution of the African and Asian monsoons during the past 30 Myr using an atmospheric general circulation model. J. Geophys. Res. 104 (D10), 11995–12018.

Gallagher, K., 2012. Transdimensional inverse thermal history modeling for quantitative thermochronology. J. Geophys. Res. 117 (B2), B02408. http://dx.doi.org/10.1029/2011JB008825.

Gourbet, L., Mahéo, G., Leloup, P.H., Paquette, J-L., Henriquet, M., Liu, X., Liu, X., 2015. Western Tibet relief evolution since the Oligo-Miocene. Gondwana Res. http://dx.doi.org/10.1016/j.gr.2014.12.003.

Hacker, B.R., Gnos, E., Ratschbacher, L., Grove, M., McWilliams, M., Sobolev, S.V., Wan, J., Zhenhan, W., 2000. Hot and dry deep crustal xenoliths from Tibet. Science 287, 2463–2466.

Haider, V.L., Dunkl, I., Eynatten, H., Von Ding, L., Frei, D., Zhang, L., 2013. Cretaceous to Cenozoic evolution of the northern Lhasa Terrane and the Early Paleogene development of peneplains at Nam Co, Tibetan Plateau. J. Asian Earth Sci. 70–71, 79–98. http://dx.doi.org/10.1016/j.jseaes.2013.03.005.

Hetzel, R., Dunkl, I., Haider, V., Strobl, M., von Eynatten, H., Ding, L., Frei, D., 2011. Peneplain formation in southern Tibet predates the India–Asia collision and plateau uplift. Geology 39 (10), 983–986. http://dx.doi.org/10.1130/G32069.1.

House, M.A., Wernicke, B.P., Farley, K.A., 1998. Dating topography of the Sierra Nevada, California, using apatites (U–Th)/He ages. Nature 396, 66–69.

Houseman, G.A., McKenzie, D.P., Molnar, P., 1981. Convective instability of a thickened boundary layer and its relevance for the thermal evolution of continental convergent belts. J. Geophys. Res. 86, 6115–6132.

Husson, L., Bernet, M., Guillot, S., Huyghe, P., Mugnier, J., Replumaz, A., Robert, X., van der Beek, P., 2014. Dynamic ups and downs of the Himalaya. Geology 42 (10), 839–842.

Kapp, P., Murphy, M.A., Yin, A., Harrison, T.M., Ding, L., Guo, J., 2003. Mesozoic and Cenozoic tectonic evolution of the Shiquanhe area of western Tibet. Tectonics 22 (4). http://dx.doi.org/10.1029/2001TC001332.

Lacassin, R., Valli, F., Arnaud, N., Leloup, P.H., Paquette, J.-L., Li, H., Tapponnier, P., Chevalier, M.-L., Guillot, S., Mahéo, G., Zhiqin, X., 2004. Large-scale geometry, offset and kinematic evolution of the Karakorum fault, Tibet. Earth Planet. Sci. Lett. 219, 255–269.

Lal, D., Harris, N.B., Sharma, K.K., Gu, Z., Ding, L., Liu, T., Dong, W., Caffe, W.M., Jull, A.J.T., 2003. Erosion history of the Tibetan Plateau since the last interglacial: constraints from the first studies of cosmogenic ^{10}Be from Tibetan bedrock. Earth Planet. Sci. Lett. 217 (1–2), 33–42. http://dx.doi.org/10.1016/S0012-821X(03)00600-9.

Leloup, P.H., Arnaud, N.O., Mahéo, G., Paquette, J.-L., Guillot, S., Valli, F., Li, H., Xu, Z., Lacassin, R., Tapponnier, P., 2012. Successive deformation episodes along the Lungmu Co zone, west-central Tibet. Gondwana Res. 21, 37–52.

Leloup, P.H., Boutonnet, E., Weinberg, R.F., Mukherjee, B.K., Tapponnier, P., Lacassin Chevalier, M-L., Li, H., Valli, F., Arnaud, N., Paquette, J.-L., 2013. Comment on "Displacement along the Karakoram fault, NW Himalaya, estimated from LA-ICP-MS U–Pb dating of offset geologic markers" published by Shifeng Wang et al. in EPSL, 2012. Earth Planet. Sci. Lett. 363, 242–245. http://dx.doi.org/10.1016/j.epsl.2012.12.012.

Liu, Q., 1993. Paleoclimat et contraintes chronologiques sur les mouvements recent dans l'Ouest du Tibet : failles du Karakorumet de Longmu Co–Gozha Co, lacs en pull-apart de Longmu Co et de Sumxi Co. Ph.D. thesis. University Paris VII (360 pp.).

Liu-Zeng, J., Tapponnier, P., Gaudemer, Y., Ding, L., 2008. Quantifying landscape differences across the Tibetan plateau: implications for topographic relief evolution. J. Geophys. Res. 113 (F4), F04018. http://dx.doi.org/10.1029/2007JF000897.

Mahéo, G., Guillot, S., Blichert-Toft, J., Rolland, Y., Pêcher, A., 2002. A slab breakoff model for the Neogenous thermal evolution of South Karakorum and South Tibet. Earth Planet. Sci. Lett. 195, 45–58.

Mahéo, G., Blichert-Toft, J., Pin, C., Guillot, S., Pêcher, A., 2009. Partial melting of mantle and crustal sources beneath the south Asian margin (south Karakorum, Pakistan): implications for the late-stage geodynamic evolution of the India–Asia convergence zone. J. Petrol. 50 (3), 427–449.

Mancktelow, N.S., Grasemann, B., 1997. Time-dependent effects of heat advection and topography on cooling histories during erosion. Tectonophysics 270, 167–195.

Matte, P., Tapponnier, P., Arnaud, N., Bourjot, L., Avouac, J.P., Vidal, Ph., Liu, Q., Pan, Y., Wang, Y., 1996. Tectonics of Western Tibet, between the Tarim and the Indus. Earth Planet. Sci. Lett. 142 (3–4), 311–330.

Maussion, F., Scherer, D., Mölg, T., Collier, E., Curio, J., Finkelnburg, R., 2014. Precipitation seasonality and variability over the Tibetan Plateau as resolved by the High Asia reanalysis. J. Climate 27 (5), 1910–1927. http://dx.doi.org/10.1175/JCLI-D-13-00282.1.

Mechie, J., Sobolev, S.V., Ratschbacher, L., Babeyko, A.Y., Bock, G., Jones, A.G., Nelson, K.D., Solon, K.D., Brown, L.D., Zhao, W., 2004. Precise temperature estimation in the Tibetan crust from seismic detection of the α–β quartz transition. Geology 32 (7), 601–604. http://doi.org/10.1130/G20367.1.

Miller, C., Schuster, R., Klötzli, U., Frank, W., Purtscheller, F., 1999. Post-collisional potassic and ultrapotassic magmatism in SW Tibet: geochemical and Sr–Nd–Pb–O isotopic constraints for mantle source characteristics and petrogenesis. J. Petrol. 40, 1399–1424.

Miller, C., Schuster, R., Klötzli, U., Frank, W., Grasemann, B., 2000. Late Cretaceous–Tertiary magmatic and tectonic events in the Transhimalaya batholith (Kailas area, SW Tibet). Schweiz. Mineral. Petrogr. Mitt. 80, 1–20.

Murphy, M.A., Yin, A., Kapp, P., Harrison, T.M., Ding, L., Guo, J., 2000. Southward propagation of the Karakoram fault system, southwest Tibet: timing and magnitude of slip. Geology 28 (5), 451–454.

Murphy, M.A., Saylor, J.E., Ding, L., 2009. Late Miocene topographic inversion in southwest Tibet based on integrated paleoelevation reconstructions and structural history. Earth Planet. Sci. Lett. 282 (1–4), 1–9. http://dx.doi.org/10.1016/j.epsl.2009.01.006.

Pan, G.T., Ding, J., Yao, D.S., Wang, L.Q., 2004. Geological Map of Qinghai–Xizang (Tibet) Plateau and Adjacent Areas. Chengdu Cartographic Publishing House, Chengdu, Chengdu Institute of Geology and Mineral Resources, China Geological Survey, scale 1/1,500,000.

Phillips, R.J., Parrish, R.R., Searle, M.P., 2004. Age constraints on ductile deformation and long-term slip rates along the Karakoram fault zone, Ladakh. Earth Planet. Sci. Lett. 226 (3–4), 305–319.

Quade, J., Breecker, D.O., Daeron, M., Eiler, J., 2011. The paleoaltimetry of Tibet: an isotopic perspective. Am. J. Sci. 311 (2), 77–115. http://dx.doi.org/10.2475/02.2011.01.

Ramstein, G., Fluteau, F., Besse, J., Joussaume, S., 1997. Effect of orogeny, plate motion and land–sea distribution on Eurasian climate change over the past 30 million years. Nature 386, 788–795.

Raterman, N.S., Cowgill, E., Lin, D., 2007. Variable structural style along the Karakoram fault explained using triple junction analysis of intersecting faults. Geosphere 3, 71–85. http://dx.doi.org/10.1130/GES00067.1.

Reiners, P.W., 2005. Zircon (U–Th)/He thermochronometry. Rev. Mineral. Geochem. 58 (1), 151–179. http://dx.doi.org/10.2138/rmg.2005.58.6.

Rohrmann, A., Kapp, P., Carrapa, B., Reiners, P.W., Guynn, J., Ding, L., Heizler, M., 2012. Thermochronologic evidence for plateau formation in central Tibet by 45 Ma. Geology 40 (2), 187–190. http://dx.doi.org/10.1130/G32530.1.

Sanchez, V.I., Murphy, M.A., Robinson, A.C., Lapen, T.J., Heizler, M.T., 2013. Tectonic evolution of the India–Asia suture zone since Middle Eocene time, Lopukangri area, south-central Tibet. J. Asian Earth Sci. 62, 205–220. http://dx.doi.org/10.1016/j.jseaes.2012.09.004.

Saylor, J., DeCelles, P., Quade, J., 2010. Climate-driven environmental change in the Zhada basin, southwestern Tibetan Plateau. Geosphere 6 (2), 74–92. http://dx.doi.org/10.1130/GES00507.1.

Schildgen, T.F., Balco, G., Shuster, D.L., 2010. Canyon incision propagation recorded by apatite ^{4}He/^{3}He thermochronometry. Earth Planet. Sci. Lett. 293 (3–4), 377–387.

Shackleton, R.M., Chang, C., 1988. Cenozoic uplift and deformation of the Tibetan Plateau: the geomorphological evidence. Philos. Trans. R. Soc. Lond. A 327, 365–377. http://dx.doi.org/10.1098/rsta.1988.0134.

Shen, T., Wang, G., Leloup, P.H., van der Beek, P., Bernet, M., Cao, C., Wang, A., Liu, C., Zhang, K., 2016. Controls on Cenozoic exhumation of the Tethyan Himalaya from fission-track thermochronology and detrital zircon U–Pb geochronology in the Gyirong basin area, southern Tibet. Tectonics 35. http://dx.doi.org/10.1002/2016TC004149.

Shuster, D.L., Farley, K.A., 2004. ^{4}He/^{3}He thermochronometry. Earth Planet. Sci. Lett. 217 (1–2), 1–17.

Shuster, D.L., Farley, K.A., Sisterson, J.M., Burnett, D.S., 2004. Quantifying the diffusion kinetics and spatial distributions of radiogenic ^{4}He in minerals containing proton-induced ^{3}He. Earth Planet. Sci. Lett. 217 (1–2), 19–32. http://dx.doi.org/10.1016/S0012-821X(03)00594-6.

Shuster, D.L., Flowers, R.M., Farley, K.A., 2006. The influence of natural radiation damage on helium diffusion kinetics in apatite. Earth Planet. Sci. Lett. 249 (3–4), 148–161.

Strobl, M., Hetzel, R., Niedermann, S., Ding, L., Zhang, L., 2012. Landscape evolution of a bedrock peneplain on the southern Tibetan Plateau revealed by in situ-produced cosmogenic ^{10}Be and ^{21}Ne. Geomorphology 153–154, 192–204. http://dx.doi.org/10.1016/j.geomorph.2012.02.024.

Tapponnier, P., Molnar, P., 1977. Active faulting and tectonics in China. J. Geophys. Res. 82, 2905–2930.

Tapponnier, P., Peltzer, G., Le Dain, A.Y., Armijo, R., Cobbold, P., 1982. Propagating extrusion tectonics in Asia: new insights from simple experiments with plasticine. Geology 10, 611–616.

Tremblay, M.M., Fox, M., Schmidt, J.L., Tripathy-Lang, A., Wielicki, M.M., Harrison, T.M., Zeitler, P.K., Shuster, D.L., 2015. Erosion in southern Tibet shut down at ~10 Ma due to enhanced rock uplift within the Himalaya. Proc. Natl. Acad. Sci. USA 112 (39). http://dx.doi.org/10.1073/pnas.1515652112.

Turcotte, D.L., Schubert, G., 2002. Geodynamics. Cambridge Univ. Press, New York, 456 pp.

Turner, S., Arnaud, N., Liu, J., Rogers, N., Hawkesworth, C., Harris, N., Kelley, S., VanCalsteren, P., Deng, W., 1996. Post-collision, shoshonitic volcanism on the Tibetan plateau: implications for convective thinning of the lithosphere and the source of ocean island basalts. J. Petrol. 37, 45–71.

Valli, F., Arnaud, N., Leloup, P.H., Sobel, E.R., Mahéo, G., Lacassin, R., Guillot, S., Haibing, L., Tapponnier, P., Xu, Z., 2007. Twenty million years of continuous deformation along the Karakorum fault, western Tibet: a thermochronological analysis. Tectonics 26 (4). http://dx.doi.org/10.1029/2005TC001913.

Valli, F., Leloup, P.H., Paquette, J.-L., Arnaud, N., Li, H., Tapponnier, P., Lacassin, R., Guillot, S., Liu, D., Deloule, E., Mahéo, G., 2008. New U–Th/Pb constraints on timing of shearing and long-term slip-rate on the Karakorum fault. Tectonics 27 (5). http://dx.doi.org/10.1029/2007TC002184.

Van Buer, N.J., Jagoutz, O., Upadhyay, R., Guillong, M., 2015. Mid-crustal detachment beneath western Tibet exhumed where conjugate Karakoram and Longmu–Gozha Co faults intersect. Earth Planet. Sci. Lett. 413, 144–157. http://dx.doi.org/10.1016/j.epsl.2014.12.053.

van der Beek, P., Van Melle, J., Guillot, S., Pêcher, A., Reiners, P.W., Nicolescu, S., Latif, M., 2009. Eocene Tibetan plateau remnants preserved in the northwest Himalaya. Nat. Geosci. 2 (5), 364–368. http://dx.doi.org/10.1038/ngeo503.

Wang, S., Wang, C., Phillips, R.J., Murphy, M.A., Xiaomin, F., Yahui, Y., 2012. Displacement along the Karakoram Fault, NW Himalaya, estimated from LA-ICP-MS U–Pb dating of offset geologic markers. Earth Planet. Sci. Lett. 337–338, 156–163.

Willett, S.D., McCoy, S.W., Perron, J.T., Goren, L., Chen, C.-Y., 2014. Dynamic reorganization of river basins. Science 343 (6175), 1248765. http://dx.doi.org/10.1126/science.1248765.

Williams, H.M., Turner, S.P., Pearce, J.-A., Kelley, S.P., Harris, N.B.W., 2004. Nature of the source regions for post-collisional, potassic magmatism in Southern and Northern Tibet from geochemical variations and inverse trace element modelling. J. Petrol. 45 (3), 555–607. http://dx.doi.org/10.1093/petrology/egg094.

Wolf, R.A., Farley, K.A., Kass, D.M., 1998. Modeling of the sensitivity of the apatite (U–Th)/He thermochronometer. Chem. Geol. 148, 105–114.

Yatagai, A., Kamiguchi, K., Arakawa, O., Hamada, A., Yasutomi, N., Kitoh, A., 2012. APHRODITE: constructing a long-term daily gridded precipitation dataset for Asia based on a dense network of rain gauges. Bull. Am. Meteorol. Soc. 93 (9), 1401–1415. http://dx.doi.org/10.1175/BAMS-D-11-00122.1.

Zhao, T.-P., Zhou, M.-F., Zhao, J.-H., Zhang, K.-J., Chen, W., 2008. Geochronology and geochemistry of the ca. 80 Ma Rutog granitic pluton, northwestern Tibet: implications for the tectonic evolution of the Lhasa Terrane. Geol. Mag. 145 (06), 845–857. http://dx.doi.org/10.1017/S0016756808005025.